Probing molecular layers with low-energy electrons

Tebyani, A.

7

Low Energy Electron Microscopy at Cryogenic Temperatures *

Abstract

We describe a cryogenic sample chamber for low energy electron microscopy (LEEM), and present first experimental results. Modifications to our IBM/SPECS aberration-corrected LEEM instrument are presented first. These include incorporation of mechanisms for cooling the sample and its surroundings, and reduction of various sources of heat load. Using both liquid nitrogen and liquid helium, we have reached sample temperatures down to about 15 K. We also present first results for low-temperature LEEM, obtained on a three-monolayer pentacene film. Specifically, we observe a reduction of the electron beam irradiation damage cross-section at 15 eV by more than a factor of five upon cooling from 300 K down to 52 K. We also observe changes in the LEEM-IV spectra of the sample upon cooling, and discuss possible causes.

* This chapter has been published as "Low energy electron microscopy at cryogenic temperatures", A. Tebyani, S. Schramm, M. Hesselberth, D. Boltje, J. Jobst, R.M. Tromp, S.J. van der Molen - Ultramicroscopy 253, 113815 (2023)

Chapter 7

7.1 Introduction

Since its realization in 1985 [1], low-energy electron microscopy (LEEM) has been successfully employed to study a plethora of surface phenomena, in particular for real-time observation of dynamic processes at surfaces including phase transitions and growth of a large variety of materials such as molecular layers, oxide films, metals, two-dimensional materials, etc. [2–15] Advancements such as the addition of aberration-correction [16–18], spin-polarization of the electron beam [19,20] and the possibility for complementary imaging with low-energy electrons transmitted through the sample (eV-TEM) [21] have further enhanced the capabilities of LEEM. Moreover, various other techniques related to LEEM have made it possible to not only investigate the microstructure of the sample surface in real and reciprocal space, but also to extract information about other properties (such as electronic band structure) and perform various forms of spectroscopy. Some examples include photoemission electron microscopy (PEEM) and angle-resolved photoemission spectroscopy (ARPES), energy filtering and electron energy loss spectroscopy (EELS) [22–25], angle-resolved reflected-electron spectroscopy (ARRES) [26,27] and low energy electron potentiometry (LEEP) [28].

So far, LEEM measurements have mostly been performed on samples with temperatures above room temperature. However, there have been a number of reports of LEEM operation at cryogenic temperatures. In 2000, Tober et. al. reported the first spin-polarized LEEM images obtained below room temperature (at 118 K) on Co thin films grown on Au(111), using a liquid-nitrogen-cooled spin-polarized LEEM instrument [29]. Some other examples include measurements of magnetic transitions in ultrathin Fe films on Cu(100) down to 248 K [8], growth of indium on Si(111) down to -100˚C [14], the Verwey transition of the magnetic material Fe_3O_4 down to 100 K [7,30], evolution of magnetic domains of a Tb film on W(110) cooled down to 80 K [31], and the report of sample temperatures >100 K reached in the ALBA LEEM instrument [32]. Meanwhile, advancements in instrumentation have been reported in similar (cathode-lens based) microscopy techniques, extending the range of available sample temperatures into cryogenic temperatures. For example, in 2012, Doran et. al. reported an X-ray PEEM (X-PEEM) instrument capable of imaging down to 25 K. [33] In 2015, Tusche et. al. reported a spin resolving microscope, with cathode objective lens design, capable of high resolution imaging of the momentum distribution of photoelectrons down to 18 K [34]. More recently, G. Schönhense et. al. have reported electronic band mapping of various materials such as $TiTe_2$, Mo, Re, $YbRh_2Si_2$ and W(110), using X-ray photoelectron microscopy down to 20-30 K [35–38]. Some other examples of PEEM and X-ray Magnetic Circular Dichroism (XMCD) measurements at cryogenic temperatures include evolution of magnetic domains of Fe_3GeTe_2 down to 110 K [39], structural phase

transition of V_2O_3 down to 150 K [40], imaging of a superconducting-ferromagnet hybrid at 45 K [41], linear dichroism of FeSe at 11 K and $BaFe_2(As_{0.87}P_{0.13})_2$ at 65 K [42], growth of anthracene layers on silicon at ~ -40˚C [6], and measurements on van der Waals ferromagnet Fe_5GeTe_2 down to 50 K [43], among others.

Here, we present a cryogenic sample chamber, incorporated into the aberration-corrected IBM/SPECS LEEM instrument [16,17]. It has the capability to cool the sample to controllable cryogenic temperatures down to ~15 K. Our design is compatible with the stringent requirements imposed by the nature of LEEM. Such requirements include the fact that the sample itself is biased with a voltage of -15 kV (as it acts as the cathode in the cathode objective lens). Furthermore, vibrations from the cooling mechanism are not to compromise the desired imaging resolution. Next, we present our first results for low-temperature LEEM on a three-monolayer pentacene film.

7.2 Experimental Technique

The cryogenic sample chamber is incorporated in the ESCHER LEEM instrument at Leiden University, an aberration-corrected IBM/SPECS LEEM instrument. [16,17] The overall design has previously been reported in Ref. [44]. As shown in Fig. 7.1, in ESCHER, the central illumination and projector column is shared between a room/high-temperature sample chamber and the low-temperature chamber on which we focus here. Via the top magnetic prism we can direct the electron beam to either of the sample chambers, by controlling the current direction. The design of the cryogenic chamber resembles that of the typical room/high-temperature chamber; however, the requirements for low-temperature operation have led to various modifications, as discussed in detail below.

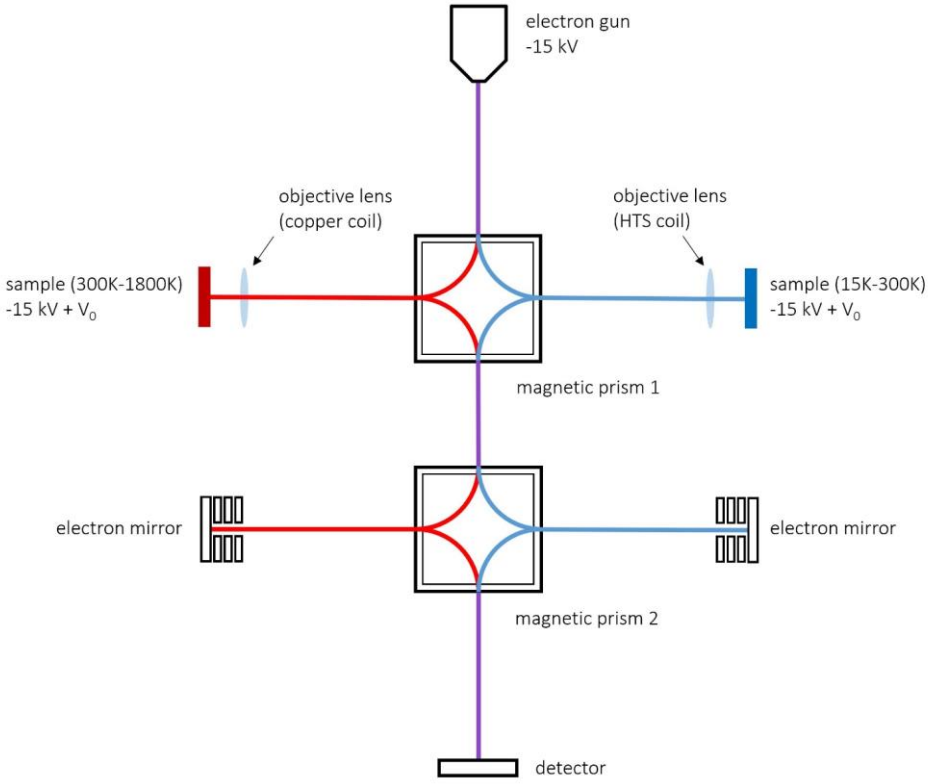

Fig. 7.1 Schematic of the ESCHER LEEM instrument. Electrons are emitted from the gun and go through the column with a kinetic energy of 15 keV. Before interaction with the sample, they are decelerated to a kinetic energy of eV_0. The beam path for the cryogenic and room/high-temperature operation is indicated in blue and red, respectively. The central column is shared between the cryogenic and room/high-temperature sides (purple beam path). To maintain the required symmetry, the two sides have separate aberration-correcting electron mirrors. The objective lens coil for the room/high-temperature side is comprised of a copper coil, while for the cryogenic side, a high-temperature superconducting (HTS) coil is used to prevent Joule heating and, hence, reduce the total heat load.

After emission from the electron gun and traversing the column with a kinetic energy of 15 keV, the electron beam is directed toward the sample (from the left in Fig. 7.1 and Fig. 7.2(a)) via magnetic prism 1. Before interacting with the sample, the incoming beam is decelerated to an energy of only a few eV, as a result of an electric field between the sample and the objective lens (~15 kV/mm). This interaction energy is tuned precisely via the sample potential. Afterwards, the reflected electrons are collected by the same electric field and, after passing through an aberration-correcting path comprising of an electron mirror, are guided toward the detector. The entire beam path is shown in Fig. 7.1. The aberration-correcting section for the cryogenic and the room/high-temperature operation are separate, as can be

seen in Fig. 7.1. Furthermore, the cryogenic chamber is equipped with its own separate load lock and sample transfer mechanism. However, sample transfer between the cryogenic and the room/high-temperature chambers without exposure of the sample to ambient conditions is not possible. The two sample chambers share the central column of the microscope, so that simultaneous measurements in the cryogenic and the room/high-temperature chambers are not possible. Alternating between measuring at either sides (i.e. on different samples) is quick and simple, however.

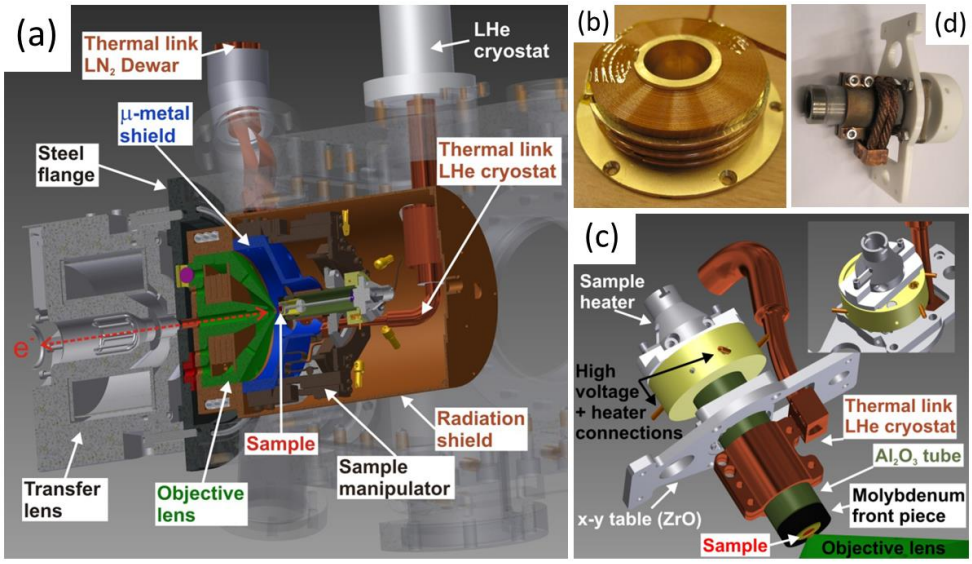

Fig. 7.2 Detailed schematic of the cryogenic sample chamber. (a) Schematic cross-section of the cryogenic setup. Electrons enter the chamber from the left. Various elements are highlighted and annotated. (b) Photograph showing the HTS coil assembly. The four disks are separated by 1-mm thick Au-plated copper plates (c) Schematic of the cryogenic sample holder, with its various components highlighted and annotated. The copper clamp around the sapphire tube is connected to the helium flow cryostat. (d) Photograph of the sample holder assembly

A detailed schematic of the cryogenic sample chamber is illustrated in Fig. 7.2(a). In the cryogenic chamber, the electromagnetic objective lens is excited by a high-temperature superconducting (HTS) coil, instead of a copper coil as used in the room/high-temperature chamber, in order to avoid Joule heating of the cryogenic set-up. The HTS assembly is comprised of a stack of four disk-shaped windings of a HTS tape (SCS3050-i, Superpower Inc.) separated by 1-mm thick Au-plated copper plates, cooled to liquid-nitrogen temperature. A picture of the HTS coil assembly, mounted to the objective lens base, is shown in Fig. 7.2(b).

Regarding heat transfer mechanisms, we are mainly concerned with minimizing radiative heat transfer through vacuum as well as conductive heat transfer through solids and solid/solid interfaces. In our design, the entire cathode objective lens and the sample stage are cooled with liquid nitrogen to a fixed temperature of ~80K. Furthermore, all these elements are enclosed in an Au-plated copper cylinder which is also cooled to the same temperature. This cylinder acts as a radiation shield against the room temperature environment, and reduces the radiative heat load on the sample holder by an estimated ~99.6% [45]. This is due to the fact that the net exchange of radiative heat is proportional to $(T_h^4 - T_c^4)$, T_h and T_c being the temperature of the hotter and colder sides of heat transfer, respectively. Placement of a cooled heat shield reduces T_h from 300K to 80K. Cooling the lens also prevents radiative heat load from an otherwise-warm lens on the sample. The cooling of all these elements is carried out via a flexible copper braid connection to a liquid nitrogen bath dewar (see Fig. 7.2(a)). The flexibility of this connection dampens the vibrations coming from the dewar, hence allowing for high-resolution imaging afforded by the aberration-correcting optics. Cooling all these elements also minimizes cryogenic pumping by the sample and has the added value of reducing thermal gradients.

Additionally, the sample itself can be cooled further via a flexible copper braid connected to a low-vibration helium flow cryostat (Advanced Research Systems Inc. LT3B), allowing for operation at further reduced temperatures. The copper braid mounted on the cold finger of the flow cryostat is clamped around a sapphire tube, at the end of which the sample (inside a molybdenum cap) is mounted. A schematic and a picture of these parts are shown in Fig. 7.2(c-d). The sapphire tube provides electrical insulation between the sample (biased at -15kV) and the flow cryostat, whilst having a relatively high thermal conductivity that increases with decreasing temperature. Only the sample and its immediate vicinity are cooled by the flow cryostat. Sample temperatures down to 15K have been achieved. The thermometer (silicon diode) for this readout is connected to the copper braid at the point of connection to the flow cryostat. Sample temperatures were calibrated with a second thermometer placed on the sample, and showed a difference of about 2K with the flow cryostat. The entire cool down process from room temperature until the microscope is operational takes about 8 hours. This time scale is dominated by the time it takes for the HTS lens to have sufficient critical current. We note that the sample itself can be cooled much faster. Also, the stabilisation time is negligible. Fig. 7.3 shows the final stage of the sample cool down (to 19K here). Cooling the sample with liquid helium via the flow cryostat while the HTS lens is being cooled can expedite reaching the required critical current in the lens. Future improvements by replacing the copper braid connection to the liquid nitrogen bath dewar with a stronger one can be expected to further reduce this waiting time. A resistive

heater element placed behind the sample can be used to heat the sample by electron bombardment up to ~1400K, allowing for *in situ* sample cleaning and preparation at elevated temperatures. Furthermore, an evaporator connected to the sample chamber allows for *in situ* deposition of various materials at ultrahigh vacuum (UHV) pressures.

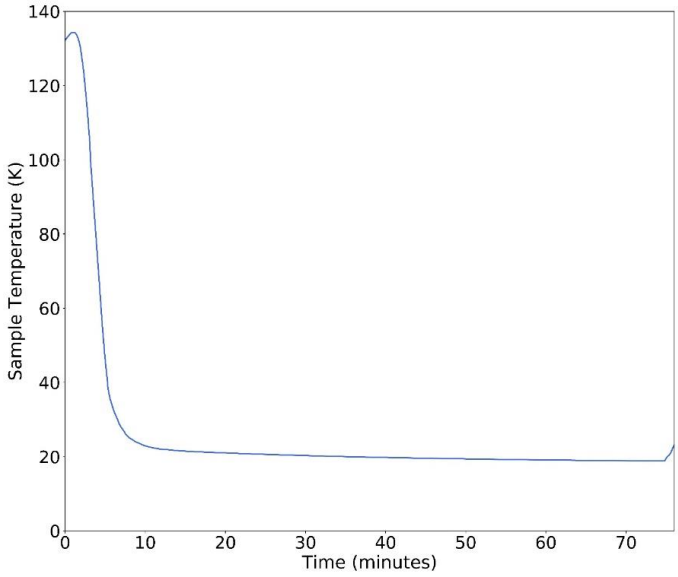

Fig. 7.3 Sample temperature during the final stage of sample cooling to 19 K. Note that the liquid He supply was stopped after 75 minutes.

The mounting of the cryogenic components has been designed such that the conductive heat transfer from the rest of the microscope (which is at room temperature) to the aforementioned liquid-nitrogen-cooled parts is minimized. We chose for mechanical mounts consisting of only three ZrO screws and four ZrO spheres, with minimal contact area with the room-temperature parts. [45] One of these spheres is colored as a purple circle behind the objective lens in Fig. 7.2(a). Finally, the sample also needs to be adjustable with five degrees of freedom: x and y in-plane movements to change the illuminated area on the sample, z-adjustment as well as two perpendicular tilt-angles to align the sample with respect to the optical axis (i.e. the illuminating electrons). These movements are powered by piezo elements in the sample stage. For low-temperature operation, the SmarAct piezomotors used at the room/high-temperature side did not suffice. Hence, new piezomotors capable of generating sufficient force at liquid nitrogen temperature, have been designed and produced in our lab. The piezomotors employ compact actuators coupled to a thermal-expansion-compensating

preload mechanism and have optimized tribological elements and compact roller bearings. The actuators in each motor are driven mutually out of phase using custom power electronics. Actuator control signals are linear ramps with a slope-matched parabolic onset. These motors, each measuring 30x17x8.5 mm, achieve a driving force of 7N at 77K. They are incorporated in the cryogenic sample stage and provide high-precision control of sample position and tilt in all directions. The piezomotors will be described in a separate publication.

7.3 Results and Discussion

First, we present a real-space image obtained in the cryogenic chamber. Figure 7.4 shows a bright-field image of a Si(111) surface, imaged at 58 K with 10.3 eV electrons. Silicon was first flashed at high temperature in order to remove the native oxide layer. Upon cooling down, the surface undergoes a 7×7 reconstruction, [46] also manifested in the diffraction pattern. The bright domains in Fig. 7.4 are a result of the surface reconstruction.

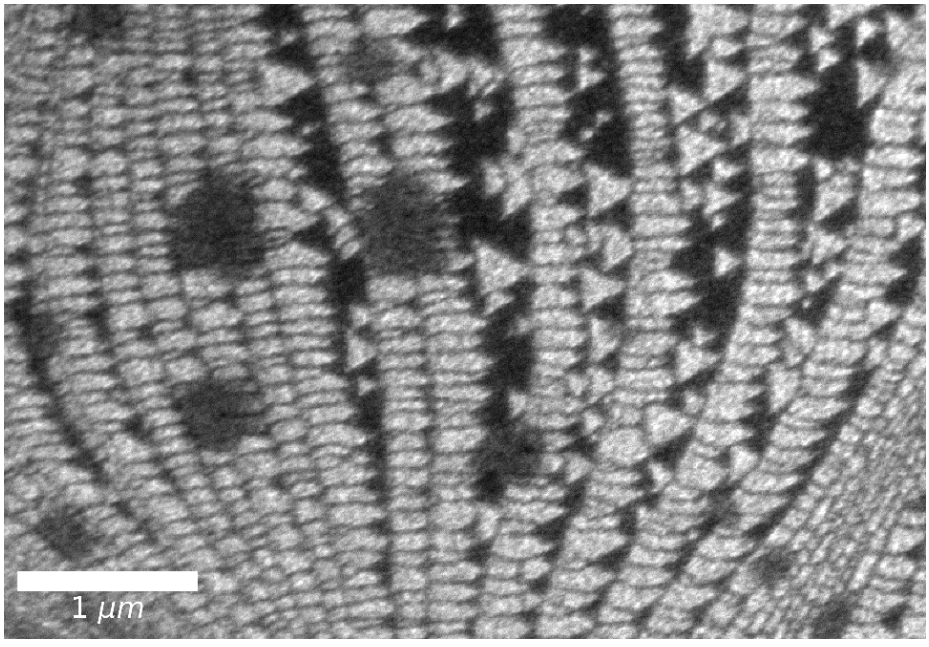

Fig. 7.4 Bright-field image of Si(111) 7×7 surface reconstruction, imaged at 58 K with 10.3 eV electrons

Next, we present the first systematic LEEM measurements within our cryogenic chamber, obtained on a pentacene film. The pentacene layers have first been grown on a Si(111) substrate via sublimation from a Knudsen cell evaporator. Growth is monitored in real-time with both LEEM and PEEM. [2,3,47] The film is covered mostly with three monolayers of pentacene, but there exist layer count variations within the beam diameter (60 μm^2), because the growth of each subsequent layer starts before the previous layer is fully finished. Since sublimation of molecules was not possible in the cryogenic chamber at the time, the sample was made in the room/high-temperature chamber and was subsequently transferred to the cryogenic chamber, with less than 30 minutes exposure to ambient atmosphere. After transfer to the cryogenic chamber and cooling down, we observe a sharp diffraction pattern corresponding to the herringbone crystal structure of pentacene (see Fig. 1.1 in chapter 1), similar to what we had observed in the room-temperature chamber after growth. Below, we show electron beam irradiation damage and spectroscopy measurements on the sample, all carried out at a range of low temperatures, in the cryogenic chamber. At low temperatures, we observed slight charging from the electron beam. Shining UV photons (from a Hg lamp connected to the chamber) during the measurements successfully counteracted the charging effect. We have established that the pentacene films are stable during prolonged Hg-UV ($h\nu$=4.9 eV) illumination.

First, we investigate electron irradiation damage to the sample. In chapter 4, [48] we examined damage to the crystalline structure of two- to four-monolayer pentacene films as a result of exposure to electrons with energies in the 0-40 eV range, and found the corresponding damage cross-section for each energy. Here, we show the results for a fixed beam energy of 15 eV, obtained at four different temperatures. The procedure followed to quantify the damage has been described in detail in Ref. [48]. In short, we observe and record the decay of the diffraction pattern of a pentacene area in real-time. Afterwards, Lorentzian curves are fitted to the line profile of the 0^{th}-order diffraction peak in each frame of the recording. Fig. 7.5 shows the evolution of the amplitudes of these Lorentzian fits over time (i.e. with accumulating dose), obtained at four different temperatures. A simple exponential fit of the form $Ae^{-\sigma \cdot D} + B$ to the data yields the damage cross-section at a given temperature and beam energy. Here, D is the accumulated dose over time in units of number of electrons per nm^2, σ is the damage cross-section in nm^2, and A and B are constants. It is evident from Fig. 7.5 that the decay of the diffraction peak intensity proceeds at a slower rate as the temperature of the sample decreases. The inset shows that the damage cross-section is reduced by a factor of ~5.4 upon cooling down from 300 K to 52 K. This is not surprising, given that in Transmission Electron Microscopy (TEM), cryogenic temperatures are used in order to reduce beam damage and extend sample lifetime. [49–52]

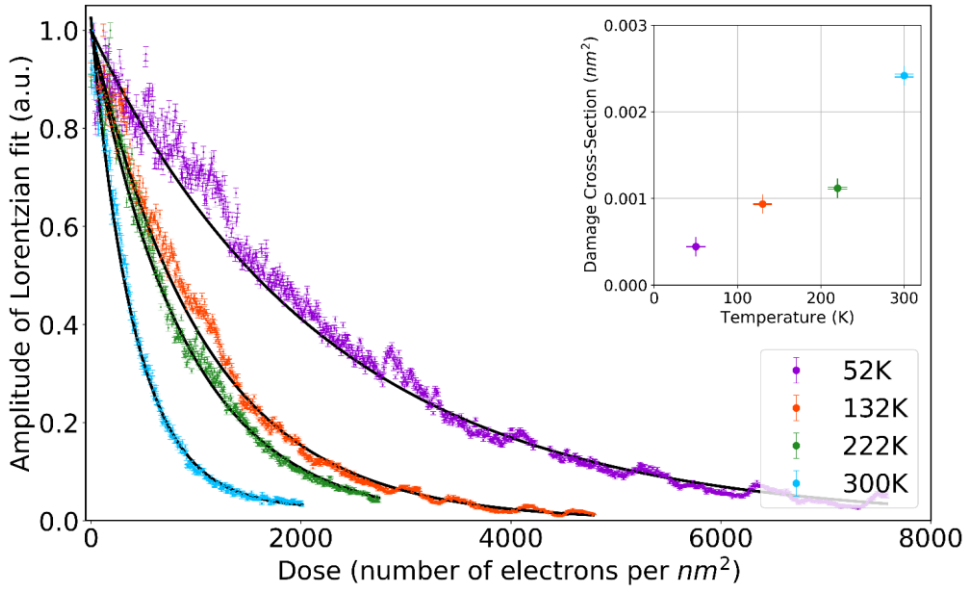

Fig. 7.5 Irradiation damage from a beam of 15 eV electrons to a pentacene film three monolayers in thickness. To quantify the damage, Lorentzian curves are fit to the spot profile of the 0^{th}-order diffraction peak. The plot shows the decay of diffraction intensity over time, as a result of accumulated dose. Beam damage is obtained at four different temperatures of 52 K, 132 K, 222 K and 300 K. The solid black curves are simple exponential fits of the form $Ae^{-\sigma \cdot D} + B$, where D is the accumulated dose (horizontal axis), σ is damage cross-section in nm^2, and A and B are constants. Cross-sections obtained from the fits are displayed in the inset figure. The colors correspond to the temperatures in the main figure legend.

The key to understanding our observations is consideration of the mechanisms that lead to damage. These include electron attachment, particularly at lower electron energies, as well as impact excitation and impact ionization (dominant at higher energies). Each of these mechanisms leads to chemical changes in the molecule and beam damage in a different way, with the activation energies for various damage mechanisms not being the same. Hence, they will likely not be suppressed equally upon cooling. Irradiation studies of self-assembled monolayers in the range 50-300 K suggest that reactions involving transport of small fragments or single atoms proceed nearly independent of temperature, while those involving transport of heavy fragments are efficiently suppressed by cooling. [53] Another beam damage study in aromatic organic single crystals reported two activation energies between 4K and 293K, with the higher-energy component ascribed to violent atomic movement and bond scission. [51]

Dissociative electron attachment is reported to be most effective in the electron energy range 5-10 eV for pentacene. [54,55] This energy range also largely coincides with the wide resonance for the excitation of the carbon-hydrogen bond in benzene from 5.5 eV to 10 eV with a shoulder at 4-5.5 eV [56], that can lead to hydrogen removal. For the beam energy of 15 eV, as used here, we expect impact excitation and ionization to be dominant, with the ionization of π-electrons starting at 6.6 eV and the ionization of σ bonds starting at 11 eV. [57–61] Given the notable temperature-dependence in the damage cross-sections observed in Fig. 7.5, it is possible that the main damage mechanism at 15 eV is fragmentation of pentacene into bigger fragments and the diffusion of those fragments, rather than scission of carbon-carbon double bonds or carbon-hydrogen bond and removal of hydrogen. However, further measurements at different beam energies are required to reach conclusions about damage at low temperatures.

Next, we study LEEM-IV spectra of pentacene as a function of temperature. As mentioned earlier, in LEEM the interaction energy of the electrons with the sample can be precisely tuned. Plotting the changes in the intensity of the 0^{th}-order diffraction peak (i.e. specularly-reflected electrons) as a function of the incident beam energy yields a so-called LEEM-IV (intensity vs. voltage) spectrum. LEEM-IV spectra are a fingerprint of the crystal and electronic band structure of the probed area, and -at low energies as used here- are predominantly determined by the unoccupied electronic density of states (DOS) above the vacuum level. [26,27,62–66] At beam energies where the DOS is high, incoming electrons can enter the sample, resulting in lower reflectivity in the LEEM-IV spectrum. Vice versa, a bandgap leads to high reflectivity. LEEM-IV spectra of the three-monolayer pentacene film obtained at different temperatures from 52 K to 300 K are plotted in Fig. 7.6. Each spectrum is obtained from a pristine area on the sample. The spectra are individually shifted (by no more than 0.3 eV) so that their mirror-mode transition energies (from full reflection to interaction with the sample) are at 0 eV; this is to compensate for slight beam tilt in the original recordings. Note that an energy of 0 eV corresponds to electrons having kinetic energy of 0 eV when they reach the sample. Negative energies imply the electrons do not have sufficient kinetic energy to reach the sample, resulting in total reflection.

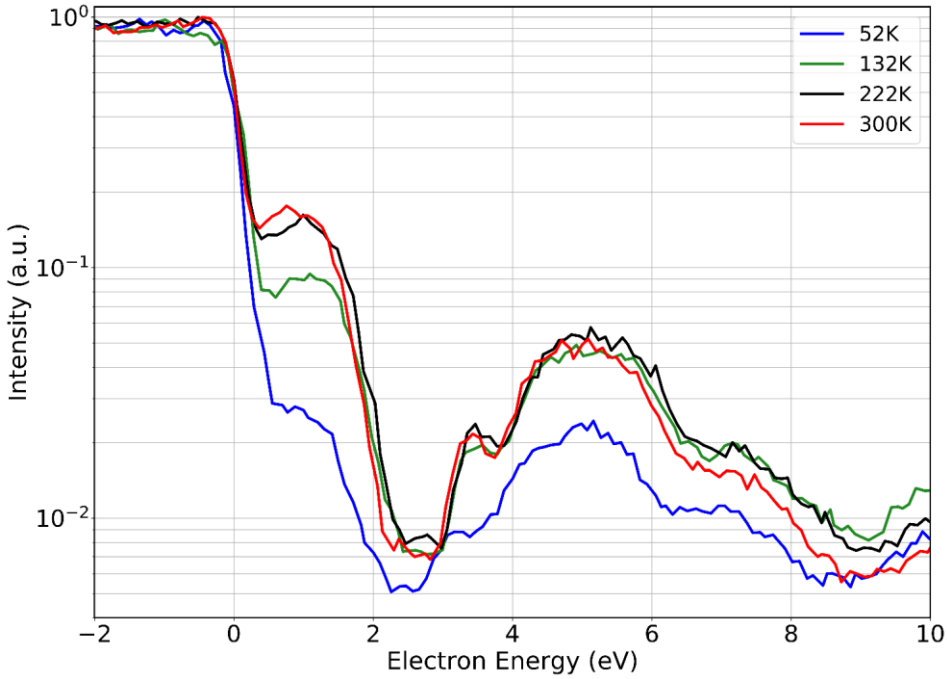

Fig. 7.6 LEEM-IV spectra of a three-monolayer pentacene film measured at different temperatures

Interestingly, in Fig. 7.6 we observe that most spectral features become weaker and less sharp upon cooling the sample. There are several possible explanations for this. The first would be the creation of disorder in the film upon cooling, as a result of the different thermal expansion coefficients between the silicon substrate and the pentacene layer. In our beam damage study [48] we observed that repeated measurements of LEEM-IV spectra on the same area lead to the diminishing and ultimate disappearance of the spectral features. The observation was attributed to irreversible chemical and structural changes to the film with increasing exposure to the beam, leading to disorder and fading of the diffraction pattern. However, in that study, all LEEM-IV features decreased in intensity with increasing damage and disorder. Here, on the other hand, a comparison of LEEM-IV spectra at 132 K and 222 K shows that while the intensity around 1 eV is lower for the LEEM-IV at 132 K, the intensity at the wide peak around 5 eV is the same for both. Another possible explanation is adsorption of contaminants on the sample surface upon cooling (note that the measurements were carried out at a pressure of ~1.0×10^{-9} mbar). However, this can be considered as another form of disorder at the surface, and hence, expected to reduce the intensity of all parts of the LEEM-IV spectra equally. Furthermore, the diffraction pattern of the sample was continuously

recorded during warm-up from 52 K up to 300 K. Line profiles of the 0^{th}-order diffraction spot in these recordings did not show any change as a function of temperature, i.e. neither widening nor sharpening. This rules out the emergence of lattice disorder and surface contamination upon cooling as causes of the changes observed in the LEEM-IV spectra in Fig. 7.6. A third possible explanation is that upon cooling, the overlap of the unoccupied molecular orbitals increases, due to contraction of the pentacene lattice. This, in turn, can lead to a broadening of the electronic bands and suppression of bandgaps. Such a development is then expected to result in lower reflectivity at lower temperatures. Note, however, that in that case, the exact changes expected will depend on the details of the electronic states and orbital overlaps. And of course, the changes in the LEEM-IV spectra could be a combination of several factors. Further measurements, for example to investigate possible changes in the dispersion of these electronic states upon cooling using ARRES [26,27], and/or to study temperature-dependent changes in electron irradiation damage cross-sections as a function of incident electron energy, are required to clarify the observations in Figs. 7.5 and 7.6.

7.4 Conclusions

We have presented the design of a cryogenic LEEM sample chamber, as well as the first results from low-temperature measurements on a pentacene film. Although similar to the room/high-temperature sample chamber of an IBM/SPECS LEEM, the low-temperature requirements lead to several design modifications to reduce the heat load, apart from the features to cool down the sample. Sample temperatures as low as 15K have been achieved, utilizing a helium flow cryostat that cools the sample and its vicinity as well as a nitrogen dewar that cools the superconducting objective lens, the entire sample stage and a radiation shield around it. Our first observations on a three-monolayer pentacene film are promising, showing a reduction in beam damage cross-section by more than a factor of 5 upon cooling from 300K to 52K, for 15 eV electrons. The LEEM-IV spectra of the sample also exhibited systematic change with temperature, although further measurements are required to conclusively explain the observations. With the cryogenic chamber, the ESCHER microscope will give access to physical phenomena over a very broad temperature range from ~15K up to 1800K, enabling novel experiments to address questions in surface science and condensed matter physics in both cryogenic and high temperatures.

References

[1] W. Telieps and E. Bauer, *An Analytical Reflection and Emission UHV Surface Electron Microscope*, Ultramicroscopy **17**, 57 (1985).

[2] Frank-J. Meyer zu Heringdorf, M. C. Reuter, and & R. M. Tromp, *Growth Dynamics of Pentacene Thin Films*, Nature **412**, 517 (2001).

[3] A. Al-Mahboob, J. T. Sadowski, Y. Fujikawa, K. Nakajima, and T. Sakurai, *Kinetics-Driven Anisotropic Growth of Pentacene Thin Films*, Phys. Rev. B **77**, 035426 (2008).

[4] J. Kautz, M. W. Copel, M. S. Gordon, R. M. Tromp, and S. J. van der Molen, *Titration of Submonolayer Au Growth on Si(111)*, Phys. Rev. B **89**, 035416 (2014).

[5] A. J. H. van der Torren, S. J. van der Molen, and J. Aarts, *Imaging Pulsed Laser Deposition Growth of Homo-Epitaxial $SrTiO_3$ by Low-Energy Electron Microscopy*, Nanotechnology **27**, 495702 (2016).

[6] N. M. Buckanie and F.-J. Meyer zu Heringdorf, *Photoemission Electron Microscopy Study of Anthracene Growth on Si(1 1 1)*, Surf. Sci. **601**, 1701 (2007).

[7] J. de la Figuera et al., *Real-Space Imaging of the Verwey Transition at the (100) Surface of Magnetite*, Phys. Rev. B **88**, 161410(R) (2013).

[8] K. L. Man, M. S. Altman, and H. Poppa, *Spin Polarized Low Energy Electron Microscopy Investigations of Magnetic Transitions in Fe/Cu(1 0 0)*, Surf. Sci. **480**, 163 (2001).

[9] H. Hibino, S. Wang, C. M. Orofeo, and H. Kageshima, *Growth and Low-Energy Electron Microscopy Characterizations of Graphene and Hexagonal Boron Nitride*, Prog. Cryst. Growth Ch. **62**, 155 (2016)

[10] H. W. Liu, H. T. Yuan, N. Fukui, L. Zhang, J. F. Jia, Y. Iwasa, M. W. Chen, T. Hashizume, T. Sakurai, and Q. K. Xue, *Growth of Topological Insulator Bi_2Te_3 Ultrathin Films on Si(111) Investigated by Low-Energy Electron Microscopy*, Cryst. Growth Des. **10**, 4491 (2010).

[11] A. Makoveev, P. Procházka, A. Shahsavar, L. Kormoš, T. Krajňák, V. Stará, and J. Čechal, *Kinetic Control of Self-Assembly Using a Low-Energy Electron Beam*, Appl. Surf. Sci. **600**, 154106 (2022).

[12] R. Zdyb, A. Locatelli, S. Heun, S. Cherifi, R. Belkhou, and E. Bauer, *Nanomagnetism Studies with Spin-Polarized Low-Energy Electron Microscopy and x-Ray Magnetic Circular Dichroism Photoemission Electron Microscopy*, Surf. Interface Anal. **37**, 239 (2005).

[13] T. Yasue, T. Koshikawa, and E. Bauer, *Low Energy Electron Microscopy/Diffraction Study on Growth of Ge on Si(113) Surface*, J. Vac. Sci. Technol. B **20**, 2496 (2002).

[14] A. Pavlovska, E. Bauer, and M. Giessen, *Low Energy Electron Microscopy Study of In on Si(111)*, J. Vac. Sci. Technol. B **20**, 2478 (2002).

[15] C. Klein, R. Ramchal, M. Farle, and A. K. Schmid, *Direct Imaging of Spin-Reorientation Transitions in Ultrathin Ni Films by Spin-Polarized Low-Energy Electron Microscopy*, Surf. Interface Anal. **38**, 1550 (2006).

[16] R. M. Tromp, J. B. Hannon, A. W. Ellis, W. Wan, A. Berghaus, and O. Schaff, *A New Aberration-Corrected, Energy-Filtered LEEM/PEEM Instrument. I. Principles and Design*, Ultramicroscopy **110**, 852 (2010).

[17] R. M. Tromp, J. B. Hannon, W. Wan, A. Berghaus, and O. Schaff, *A New Aberration-Corrected, Energy-Filtered LEEM/PEEM Instrument II. Operation and Results*, Ultramicroscopy **127**, 25 (2013).

[18] R. Wichtendahl et al., *SMART: An Aberration-Corrected XPEEM/LEEM with Energy Filter*, Surf. Rev. Lett. **5**, 1249 (1998).

[19] L. Yu et al., *Aberration Corrected Spin Polarized Low Energy Electron Microscope*, Ultramicroscopy **216**, 113017 (2020).

[20] M.S. Altman, H. Pinkvos, J. Hurst, H. Poppa, G. Marx, and E. Bauer, *Spin Polarized Low Energy Electron Microscopy of Surface Magnetic Structure*, Mater. Res. Soc. Symp. Proc. **232**, 125 (1991).

[21] D. Geelen, A. Thete, O. Schaff, A. Kaiser, S. J. van der Molen, and R. Tromp, *eV-TEM: Transmission Electron Microscopy in a Low Energy Cathode Lens Instrument*, Ultramicroscopy **159**, 482 (2015).

[22] R. M. Tromp, Y. Fujikawa, J. B. Hannon, A. W. Ellis, A. Berghaus, and O. Schaff, *A Simple Energy Filter for Low Energy Electron Microscopy/Photoelectron Emission Microscopy Instruments*, J. Phys.: Condens. Matter. **21**, 314007 (2009).

[23] Y. Fujikawa, T. Sakurai, and R. M. Tromp, *Micrometer-Scale Band Mapping of Single Silver Islands in Real and Reciprocal Space*, Phys. Rev. B **79**, 121401(R) (2009).

[24] Y. Fujikawa, T. Sakurai, and R. M. Tromp, *Surface Plasmon Microscopy Using an Energy-Filtered Low Energy Electron Microscope*, Phys. Rev. Lett. **100**, 126803 (2008).

[25] Lee H.Veneklasen, *Design of a Spectroscopic Low-Energy Electron Microscope*, Ultramicroscopy **36**, 76 (1991).

[26] J. Jobst, J. Kautz, D. Geelen, R. M. Tromp, and S. J. van der Molen, *Nanoscale Measurements of Unoccupied Band Dispersion in Few-Layer Graphene*, Nat. Commun. **6**, 8926 (2015).

[27] J. Jobst, A. J. H. van der Torren, E. E. Krasovskii, J. Balgley, C. R. Dean, R. M. Tromp, and S. J. van der Molen, *Quantifying Electronic Band Interactions in van der Waals Materials Using Angle-Resolved Reflected-Electron Spectroscopy*, Nat. Commun. **7**, 13621 (2016).

[28] J. Kautz, J. Jobst, C. Sorger, R. M. Tromp, H. B. Weber, and S. J. van der Molen, *Low-Energy Electron Potentiometry: Contactless Imaging of Charge Transport on the Nanoscale*, Sci. Rep. **5**, 13604 (2015).

[29] E. D. Tober, G. Witte, and H. Poppa, *Variable Temperature and Ex Situ Spin-Polarized Low-Energy Electron Microscope*, J. Vac. Sci. Technol. A **18**, 1845 (2000).

[30] L. Martín-García, A. Mascaraque, B. M. Pabón, R. Bliem, G. S. Parkinson, G. Chen, A. K. Schmid, and J. de la Figuera, *Spin Reorientation Transition of Magnetite (001)*, Phys. Rev. B **93**, 134419 (2016).

[31] J. E. Prieto, G. Chen, A. K. Schmid, and J. de la Figuera, *Magnetism of Epitaxial Tb Films on W(110) Studied by Spin-Polarized Low-Energy Electron Microscopy*, Phys. Rev. B **94**, 174445 (2016).

[32] L. Aballe, M. Foerster, E. Pellegrin, J. Nicolas, and S. Ferrer, *The ALBA Spectroscopic LEEM-PEEM Experimental Station: Layout and Performance*, J. Synchrotron Rad. **22**, 745 (2015).

[33] A. Doran, M. Church, T. Miller, G. Morrison, A. T. Young, and A. Scholl, *Cryogenic PEEM at the Advanced Light Source*, J. Electron. Spectrosc. **185**, 340 (2012).

[34] C. Tusche, A. Krasyuk, and J. Kirschner, *Spin Resolved Bandstructure Imaging with a High Resolution Momentum Microscope*, Ultramicroscopy **159**, 520 (2015).

[35] S. Babenkov et al., *High-Accuracy Bulk Electronic Bandmapping with Eliminated Diffraction Effects Using Hard X-Ray Photoelectron Momentum Microscopy*, Commun. Phys. **2**, 107 (2019).

[36] S. Y. Agustsson et al., *Temperature-Dependent Change of the Electronic Structure in the Kondo Lattice System $YbRh_2Si_2$*, J. Phys.: Condens. Matter. **33**, 205601 (2021).

[37] K. Medjanik et al., *Progress in HAXPES Performance Combining Full-Field k - Imaging with Time-of-Flight Recording*, J. Synchrotron. Rad. **26**, 1996 (2019).

[38] K. Medjanik et al., *Direct 3D Mapping of the Fermi Surface and Fermi Velocity*, Nat. Mater. **16**, 615 (2017).

[39] Q. Li et al., *Patterning-Induced Ferromagnetism of Fe_3GeTe_2 van der Waals Materials beyond Room Temperature*, Nano Lett. **18**, 5974 (2018).

[40] I. Valmianski, A. F. Rodríguez, J. Rodríguez-Álvarez, M. García Del Muro, C. Wolowiec, F. Kronast, J. G. Ramírez, I. K. Schuller, A. Labarta, and X. Batlle, *Driving Magnetic Domains at the Nanoscale by Interfacial Strain-Induced Proximity*, Nanoscale **13**, 4985 (2021).

[41] A. Palau et al., *Encoding Magnetic States in Monopole-Like Configurations Using Superconducting Dots*, Adv. Sci. **3**, 1600207 (2016).

[42] T. Shimojima et al., *Discovery of Mesoscopic Nematicity Wave in Iron-Based Superconductors*, Science **373**, 1122 (2021).

[43] R. Fujita, P. Bassirian, Z. Li, Y. Guo, M. A. Mawass, F. Kronast, G. van der Laan, and T. Hesjedal, *Layer-Dependent Magnetic Domains in Atomically Thin Fe_5GeTe_2*, ACS Nano **16**, 10545 (2022).

[44] S. M. Schramm, J. Kautz, A. Berghaus, O. Schaff, R. M. Tromp, and S. J. van der Molen, *Low-Energy Electron Microscopy and Spectroscopy with ESCHER: Status and Prospects*, IBM J. Res. & Dev. **55**, 1:1 (2011).

[45] S. Schramm, PhD Thesis (Leiden University): *Imaging with aberration-corrected low energy electron microscopy* (2013), ISBN: 978-90-8593-152-2. http://hdl.handle.net/1887/20843

[46] G. Binnig, H. Rohrer, C. Gerber, and E. Weibel, *7 × 7 Reconstruction on Si(111) Resolved in Real Space*, Phys. Rev. Lett. **50**, 120 (1983).

[47] F.-J. Meyer Zu Heringdorf, M. C. Reuter, and R. M. Tromp, *The Nucleation of Pentacene Thin Films*, Appl. Phys. A **78**, 787 (2004).

[48] A. Tebyani, F. B. Baalbergen, R. M. Tromp, and S. J. van der Molen, *Low-Energy Electron Irradiation Damage in Few-Monolayer Pentacene Films*, J. Phys. Chem. C **125**, 26150 (2021).

[49] B. E. Bammes, J. Jakana, M. F. Schmid, and W. Chiu, *Radiation Damage Effects at Four Specimen Temperatures from 4 to 100 K*, J. Struct. Biol. **169**, 331 (2010).

[50] K. Murata and M. Wolf, *Cryo-Electron Microscopy for Structural Analysis of Dynamic Biological Macromolecules*, BBA-Gen. Subjects **1862**, 324-334 (2018)

[51] J. R. Fryer, C. H. Mcconnell, F. Zemlin, and D. L. Dorset, *Effect of Temperature on Radiation Damage to Aromatic Organic Molecules*, Ultramicroscopy **40**, 163 (1992).

[52] L. A. Baker and J. L. Rubinstein, *Radiation Damage in Electron Cryomicroscopy*, in *Methods in Enzymology*, Jensen, G. J., Ed.; Academic Press (2010); Vol. 481, pp 371−388

[53] P. Feulner, T. Niedermayer, K. Eberle, R. Schneider, D. Menzel, A. Baumer, E. Schmich, A. Shaporenko, Y. Tai, and M. Zharnikov, *Strong Temperature Dependence of Irradiation Effects in Organic Layers*, Phys. Rev. Lett. **93**, 178302 (2004).

[54] R. V. Khatymov, R. F. Tuktarov, and M. V. Muftakhov, *Lifetime of Negative Molecular Ions of Tetracene and Pentacene with Respect to the Autodetachment of an Electron*, JETP Lett. **93**, 437 (2011).

[55] M. V. Muftakhov, R. V. Khatymov, and R. F. Tuktarov, *Decomposition of Aromatic Compounds Relevant to Organic Electronics under Exposure to Low-Energy Electrons*, Tech. Phys. **63**, 1854 (2018).

[56] R. Azria and G. J. Schulz, *Vibrational and Triplet Excitation by Electron Impact in Benzene*, J. Chem. Phys. **62**, 573 (1975).

[57] M. S. Deleuze, A. B. Trofimov, and L. S. Cederbaum, *Valence One-Electron and Shake-up Ionization Bands of Polycyclic Aromatic Hydrocarbons. I. Benzene, Naphthalene, Anthracene, Naphthacene, and Pentacene*, J. Chem. Phys. **115**, 5859 (2001).

[58] H. W. Jochims, H. Baumgärtel, and S. Leach, *Structure-Dependent Photostability of Polycyclic Aromatic Hydrocarbon Cations: Laboratory Studies and Astrophysical Implications*, ApJ **512**, 500 (1999).

[59] R. Boschi, E. Clart, and W. Schmidt, *Photoelectron Spectra of Polynuclear Aromatics. III. the Effect of Nonplanarity in Sterically Overcrowded Aromatic Hydrocarbons*, J. Chem. Phys. **60**, 4406 (1974).

[60] W. Schmidt, *Photoelectron Spectra of Polynuclear Aromatics. V. Correlations with Ultraviolet Absorption Spectra in the Catacondensed Series*, J. Chem. Phys. **66**, 828 (1977).

[61] R. Boschi, J. N. Murrell, and W. Schmidt, *Photoelectron Spectra of Polycyclic Aromatic Hydrocarbons*, Faraday Discuss. Chem. Soc. **54**, 116 (1972).

[62] J B Pendry, *The Application of Pseudopotentials to Low-Energy Electron Diffraction II: Calculation of the Reflected Intensities*, J. Phys. C: Solid State Phys. **2**, 2273 (1969).

[63] E. Bauer, *Surface Microscopy with Low Energy Electrons* (2014), Springer New York, ISBN: 978-1-4939-0934-6

[64] J. B. Pendry, *Theory of Photoemission*, Surf. Sci. **57**, 679 (1976).

[65] V. N. Strocov, E. E. Krasovskii, W. Schattke, N. Barrett, H. Berger, D. Schrupp, and R. Claessen, *Three-Dimensional Band Structure of Layered $TiTe_2$: Photoemission Final-State Effects*, Phys. Rev. B **74**, 195125 (2006).

[66] V. N. Strocov, H. I. Starnberg, and P. O. Nilsson, *Mapping the Excited-State Bands above the Vacuum Level with VLEED: Principles, Results for Cu, and the Connection to Photoemission*, J. Phys.: Condens. Matter **8**, 7539 (1996).